water

MDPI

Article

Application of Cost-Effective High-Resolution Remote Sensing to Characterize Flooding in Mountain River Corridors

Ishwar Joshi [1,2], Ian Gowing [2] and Brian M. Crookston [1,2,*]

[1] Department of Civil and Environmental Engineering, Utah State University, 8200 Old Main Hill, Logan, UT 84322, USA; ishwar.joshi@usu.edu
[2] Utah Water Research Laboratory, Utah State University, 1600 Canyon Road, Logan, UT 84321, USA; ian.gowing@usu.edu
* Correspondence: brian.crookston@usu.edu

Abstract

This study evaluated a cost-effective UAV-based multi-sensor approach for characterizing river corridor conditions during and after moderate floods in two mountain river corridors in Northern Utah, USA: the Logan River and Blacksmith Fork River. These study reaches included urban, rural, and agricultural areas, hydraulic structures and bridges, and fish passage structures. A DJI Matrice 300 UAV was used with two separate payloads: an AgEagle Altum-PT multispectral camera and an R3 Pro V2 two-return LiDAR system. The workflow included UAV flight planning and data collection, post-processing of the multi-spectral and LiDAR sensor data, spatial resolution and accuracy assessment, and interpretation of the resultant data. The multi-spectral post-processing produced pansharpened orthomosaics with a spatial resolution of 0.0432 m, while the UAV LiDAR produced DSM/DTM products at 0.05 m resolution. LiDAR accuracy assessment showed vertical RMSE values of approximately 0.0602 m for the Blacksmith Fork and 0.0782 m for the Logan River. The results showed that multispectral imagery and 2-band LiDAR provided a cost-effective means for detailed remote sensing with each sensor providing complementary information for flood and river corridor assessment. Multispectral imagery supported interpretation of flood extent, vegetation condition, relative turbidity, and thermal patterns, while LiDAR captured terrain and surface features such as banks, levees, floodplain surfaces, channel modifications, and structures. The integrated datasets supported maximum flood extent mapping and flood-level estimation. These datasets can support reach-scale hydraulic modeling, catchment hydrology, river corridor ecology, floodplain conditions, and real-time monitoring of floods, in addition to quantification of flood hazards or post-flood impacts for municipalities and insurers.

Keywords: two-return LiDAR; multi-spectral imaging; flooding; 3D mapping

Check for updates

Academic Editor: Chang Huang

Received: 4 May 2026
Revised: 24 June 2026
Accepted: 9 July 2026
Published: 21 July 2026

Copyright: © 2026 by the authors. Licensee MDPI, Basel, Switzerland. This article is an open access article distributed under the terms and conditions of the Creative Commons Attribution (CC BY) license.

1. Introduction

The demand for sustainable river corridor management and flood-risk efforts continue to increase as communities wrestle with various water-related problems, including natural disasters in watersheds [1,2]. River corridors are the lifelines of civilization that provide water conveyance, navigation, energy, habitat, and other vital resources [3–5]. Additionally, both rural and urban areas rely heavily on the resiliency of these waterways to diverse stresses and threats that include anthropogenic activities, pollution, shifting hydrologic patterns, and floods [6–9].

Therefore, there is a strong motivation to manage and conserve the channels, floodplains, and wetlands that comprise these river corridors and their corresponding resources. Such efforts may focus on sediments, nutrients, habitat, ecology, water quality and quantities, and the services provided by resident water infrastructure. However, often funding and spatial data are limited, thus monitoring and detecting river corridor responses to these efforts and any external influences are not only a challenge but also essential to formulate specific conservation strategies and assess their effectiveness [10–12].

Remote sensing techniques provide nonintrusive information used to characterize river corridor hydro-morphology across a range of scales and to discern their physical processes [13]. Various technologies allow wide spatial coverage, repeatability, in-depth resolution, dataset homogeneity, and in some instances rapid acquisition [14–16]. Speaking generally, these include various detectors [17], profilers [18], sounders [19], laser scanners [20], radars [21], satellites [16], and imagers [22] that may be fixed, handheld, or mounted to vehicles and which may be used independently or part of a multiplatform configuration [23–25].

Specifically, small unmanned aerial vehicles (UAVs) have unique capabilities for light and compact sensor payloads. Although they may not have the same spatial coverage as piloted aircraft or satellite imagery, small UAVs can offer much higher resolutions for reach-scale studies, particularly during or immediately following a specific river event (as field conditions permit). Certainly, the dominant focus with UAVs has been aerial imagery and photogrammetry techniques (Structure for Motion) to generate digital terrain models (DTMs) [26,27]. This imagery has redundant coverage (overlap) and may be used for a variety of purposes and modeling objectives not limited to flood risk assessment, river restoration, development planning, insurance claims, etc. Characterizing vegetation, biomass, river morphology, water temperatures, flow resistance metrics, and even sediment grain size and distributions are becoming more commonplace as sensor and computing capabilities continue to advance.

A growing trend is to use UAVs to study fluvial processes and river dynamics, including estimating river discharges and surface velocities without tracking particles or tracers [28–30]. Furthermore, it is also feasible to estimate the transport (source, travel paths, and areas of deposition) of many objects in rivers, such as sediment and driftwood, contaminants and pollutants, and flood debris (e.g., plastics, home goods, vehicles, homes, etc.).

However, light detection and ranging (LiDAR) sensors offer multiple distinct advantages over sensors that capture aerial photography [31]. Nevertheless, the typical tradeoff is that LiDAR sensors tend to be significantly more expensive to purchase and operate. Also, they tend to be a much heavier payload that traditionally could only be carried by manned aircraft or by larger more expensive UAVs. LiDAR sensors are known for high accuracy and having some vegetation penetration, or in the case of green LiDAR, penetrate water surfaces for bathymetric surveys. They are not light-dependent; flights can be performed at any time of day, including at night (if permitted). Post-processed LiDAR using published techniques provides intricate details captured in a dense three-dimensional point cloud, but with limited texture and color information as compared to aerial imagery. An example is provided in Figure 1 of the mouth of the Bear River with the Great Salt Lake, which is experiencing multiple water-related challenges.

In order to explore the combined usage of aerial imagery and LiDAR for reach-scale remote sensing during moderate floods caused by spring runoff, this study selected the AgEagle Altum-PT multispectral camera (manufactured by EagleNXT in Allen, TX, USA) and the R3 Pro Rock Robotics v2 LiDAR/Camera package (two returns) (manufactured by ROCK Robotics, Denver, CO, USA) and the DJI Matrice 300 UAV platform (manufac-

tured by SZ DJI Technology Co, Ltd. in Shenzhen, China). The rivers flooded were the Logan River and Blacksmith River; in addition to flooding, these river corridors have also experienced recent urbanization activities and nature conservation projects. The primary objectives of this study are: (1) how multi-spectral imagery and two-return LiDAR may complement each other to remotely monitor river corridors at high resolution, (2) the technical details associated with these technologies and UAV missions, and (3) the implications of these classes of technologies, with limited supplemental field data, for river corridor conservation studies.

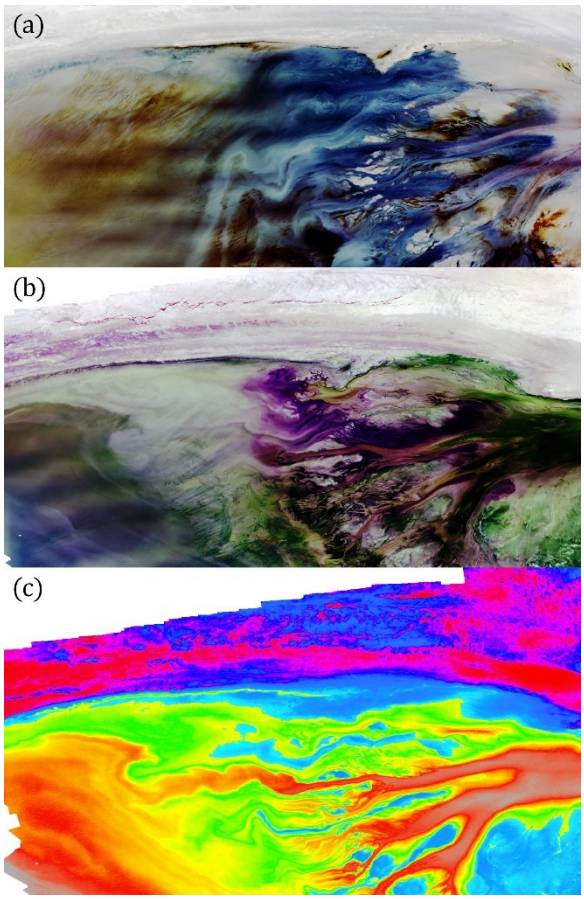


Figure 1. Confluence of the Bear River and the Great Salt Lake via aerial imagery obtained using UAV based multi-spectral cameras at 0.5 fps at 350 m elevation flown at 80 kph with (**a**) green–green–red spectra, (**b**) red–green–blue spectra, and (**c**) the thermal band. Images courtesy Brian Crookston.

2. Study Area Description

The Logan and Blacksmith Fork Rivers considered herein are in Northern Utah, USA, as shown in Figure 2. The Blacksmith Fork River is a tributary of the Logan River; corresponding river catchments are mountainous with cold, snowy winters and warm, dry summers (typically −8 °C to 32 °C). These catchments are a compilation of agricultural lands and expanding rural and urban areas with numerous hydraulic structures and floodplain encroachment within their river corridors. Due to the transition of characteristics of the Logan River from near the mouth of Logan Canyon to the flat areas of Cache Valley, this river reach is characterized by two sections split by the Main Street River Gaging Station. This study does not consider the Logan River beyond Mendon Road where it transitions into a heavily meandered section with ponds and wetlands before joining the Little Bear River and ultimately feeding Cutler Reservoir. The studied length of the Logan

River between Logan Canyon and Main Street is 4.0 km; from Main Street to Mendon Road, it is 7.5 km; the Blacksmith Fork River reaches 1.5 km.

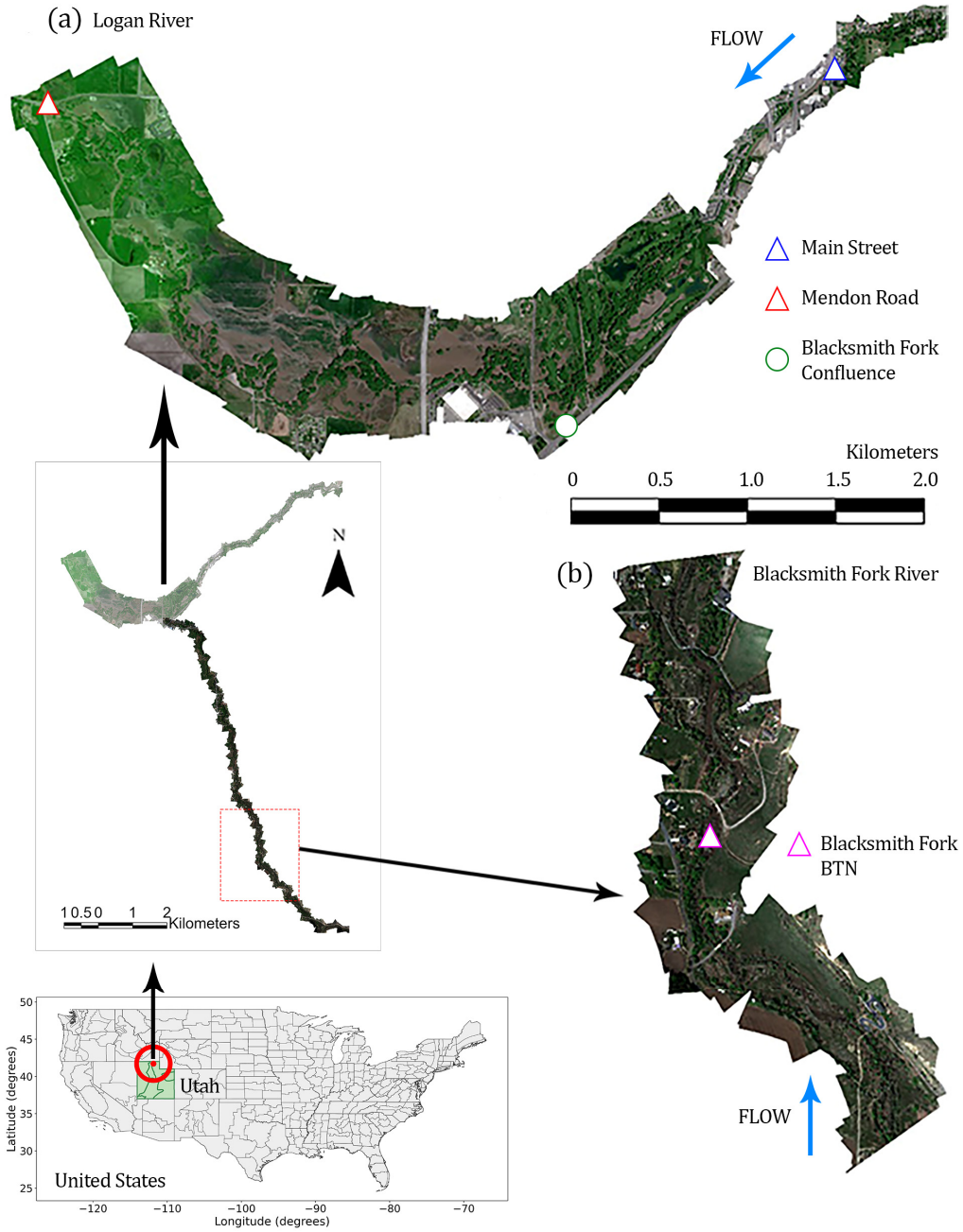


Figure 2. Overview of the study area with (**a**) Logan River reach and (**b**) Blacksmith Fork River reach.

Upstream of the Blacksmith–Logan confluence, the Main Street gaging station on the Logan River has a drainage area of about 560 km^2 with a mean basin slope of 32.9%, a mean elevation of 2292 m, and a mean annual precipitation of 896 mm [32]. Further downstream at Mendon Road, the Logan River drains a catchment area of 1370 km^2, with a mean basin slope of 31.1%, a mean elevation of 2200 m, and a mean annual precipitation of 792 mm [33]. At the Blacksmith Fork BTN gaging station (Figure 2), the Blacksmith Fork River drains a catchment area of approximately 700 km^2, with a mean basin slope of 29.8%, a mean elevation of 2173 m, and a mean annual precipitation of 736.6 mm [34].

The discharge, temperature, and sediment characteristics in these two river reaches are shown in Figure 3 (Logan River) and Figure 4 (Blacksmith Fork River). The Logan River

Reach has a gradient of 0.0058 between Main Street and Blacksmith Fork confluence and is fairly straight with a sinuosity index of 1.05. However, downstream of the confluence the river gradient is 0.0021 and is highly meandering with sinuosity index of 1.85. The Blacksmith Fork reach has a gradient of 0.0071 and is straight to meandering with sinuosity index of 1.2.

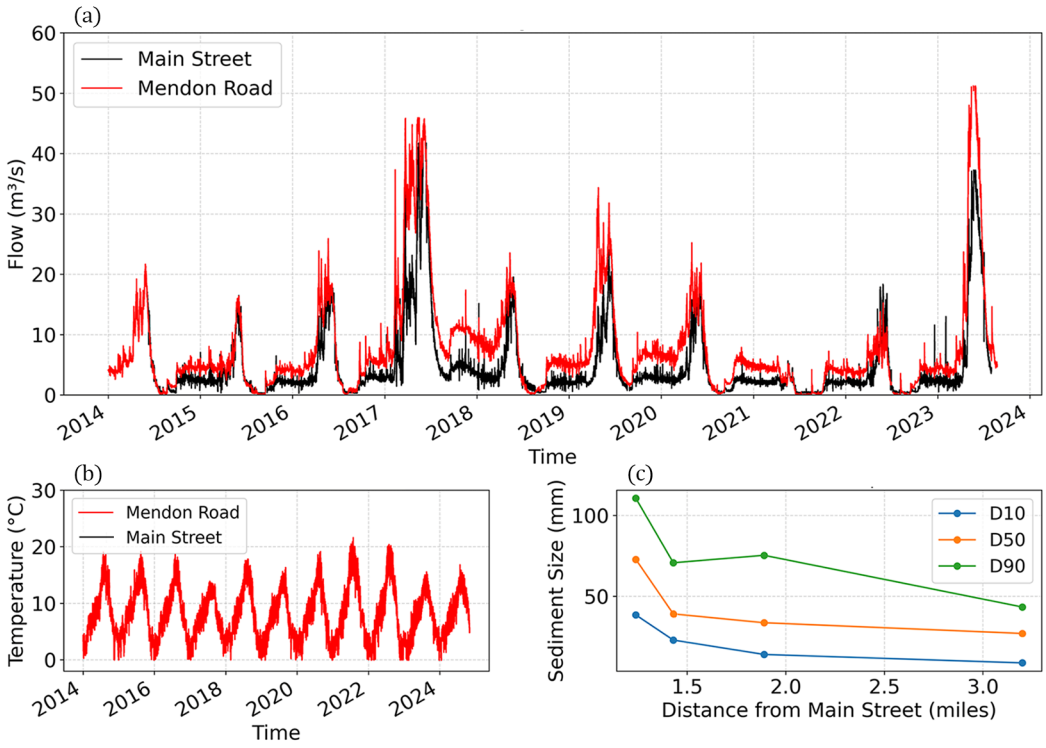


Figure 3. The Logan River reach with (**a**) streamflow measurements, (**b**) water temperatures at two hydrologic measurement stations(note that the Main Street Data is behind the Mendon Road Data), and (**c**) sediment sampling at four locations. The streamflow and water temperature data were obtained from gaging station setup by Logan River Observatory (LRO) [32] at Mendon Road and Main Street. Sediment sampling was performed by the authors at the end of 2023, and analyses were done at Utah Water Research Laboratory.

Both river reaches are not pristine with human interventions in their corridors such as bridges, water intake structures, irrigation diversions, fish passage structures, bank protection and armoring, and very recent housing developments within the floodplain. Similar to the catchment composition, the floodplain of the Logan River Reach between Main Street and Blacksmith Fork Confluence is highly urbanized with residential buildings and recreational parks. However, downstream of the confluence, the floodplain consists of predominantly agricultural land. For the Blacksmith Fork, the floodplain is partially urbanized with residential buildings on large plots of land. In addition to these interventions, there are possibilities of future wildfire-related sediment transport in these river systems affecting the hydrology, morphology, and ecology of these rivers.

Spring runoff in both rivers often leads to localized flooding and sediment and wooden debris exchanged between the main channel and floodplain. However, in years of heavy snowfall, flooding can be moderate to severe. Herein, this study considered a moderate flood event that occurred in 2023 that caused economic damages, including impacts to agricultural lands, recreational areas, private residences, and roadways.

In addition to flood conveyance, these rivers are valuable natural resources and recreational destinations. Both river corridors host a variety of native species of flora and fauna that are sensitive to changing river corridors due to natural, climatic, and

anthropogenic activities. Recent conservation actions in the Blacksmith Fork River included restoring fish passage connectivity by modifying water intake structure and constructing a series of rock weirs [35]. However, the river was also dredged of gravel recently in an effort to increase conveyance, but this did not consider the active annual bedloads and river morphology or anticipate the river's response. In the Logan River, the current conservation action plan prioritizes management and consumption of river resources that are economically viable and socially beneficial [36].

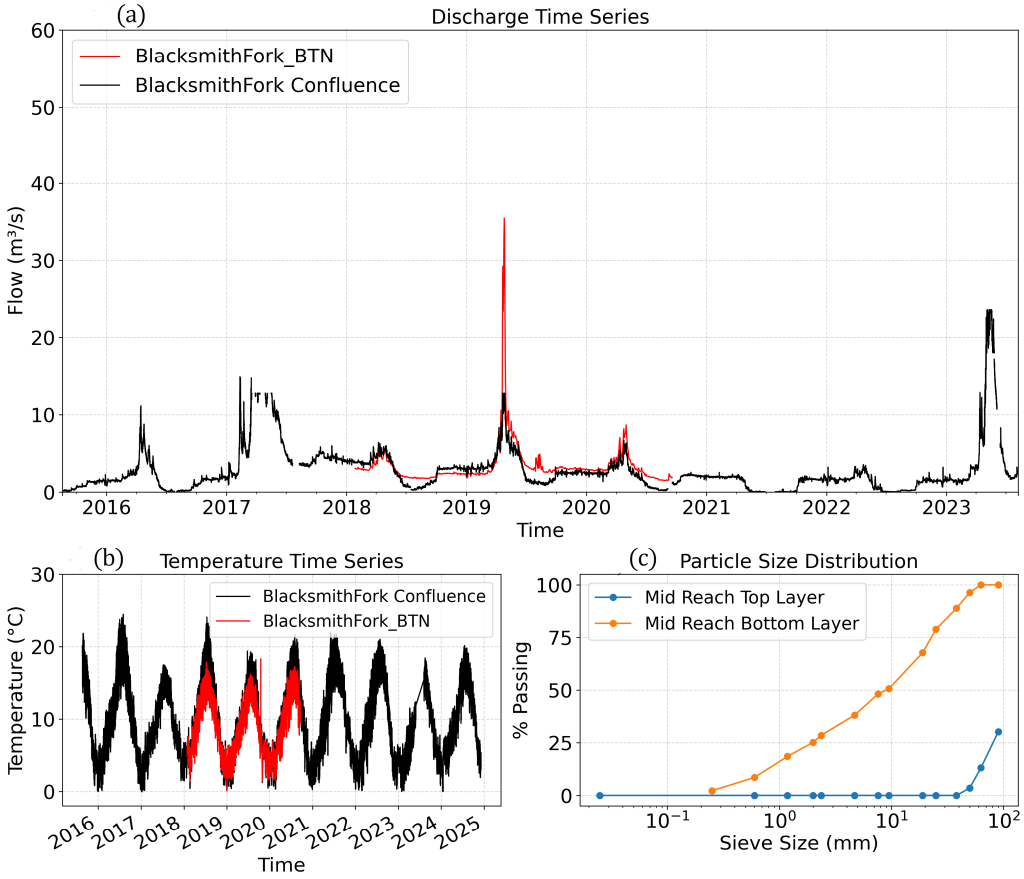


Figure 4. The Blacksmith River reach with (**a**) streamflow measurements, (**b**) water temperature, and (**c**) sediment distribution. The streamflow and water temperature data were obtained from gaging station setup by (LRO) [34] at Blacksmith Fork Confluence and BlacksmithFork_BTN. Sediment sampling was performed by the authors at the end of 2023, and analysis was done at Utah Water Research Laboratory.

3. Materials and Methods

To obtain river corridor information during moderate flooding and corresponding impacts, a multi-spectral camera and a 2-return LiDAR system were selected. For full transparency, the specific setup is disclosed herein. These sensors were mounted to a DJI Matrice 300 UAV (see Figure 5), which was selected as the UAV platform because it is an industrial-grade aircraft with sufficient payload capacity (2.7 kg), flight endurance, and stability to carry mapping sensors during repeated field surveys. According to DJI specifications, the platform has a maximum flight time of up to 55 min and supports multiple mapping payload configurations, making it suitable for separate multispectral and LiDAR flights [37]. Details of each sensor, the UAV flights and supporting field data, and post-processing are detailed herein.



Figure 5. Sensors used in this study: (**a**) AgEagle Altum-PT multi-spectral camera mounted on a DJI Matrice 300 UAV, (**b**) RS3 Reach EMLID Base station with Propeller aeropoint ground control target (GCP), and (**c**) R3 Pro Rock Robotics v2 LiDAR mounted on a DJI Matrice 300 UAV (photos courtesy Ishwar Joshi). The RS3 Reach EMLID base station is used to correct the position of the LiDAR data points during post processed kinematics (PPK) processing. The base station is not used to correct the position of the multi-spectral sensor in this research.

3.1. Multi-Spectral Camera

The multi-spectral imaging camera was AgEagle Altum-PT (Figure 6), which can capture five discrete spectral bands and one thermal band at 2 Hz, summarized in Table 1. It is a light-weight camera at only 0.577 kg. The camera also has a panchromatic sensor that enhances the resolution of the five spectral bands. This camera offers a unique advantage over other remote sensing cameras [38] due to its lightweight design and its ability to simultaneously capture visible, infrared, and thermal bands every 0.5 s.



Figure 6. Image of an AgEagle Altum-PT camera (image courtesy Ian Gowing).

Table 1. Spectral and Thermal band captured by Altum-PT camera.

Bands	Color	Range
Spectral	Blue	443–507 nm
	Green	533–587 nm
	Red	654–682 nm
	Red Edge	705–729 nm
	Near-IR	785–899 nm
Thermal	FLIR LWIR thermal infrared	7.5–13.5 µm (radiometrically calibrated)

The multispectral camera is powered via the Matrice batteries, with an additional cable leading from the camera to the Downwelling Light Sensor (DLS) situated on top of the drone (manufactured by EagleNXT, Allen, TX, USA). The DLS improves reflectance calibration during changing light conditions of a flight mission and records this information in the metadata of each TIFF image. In this research, the Altum PT captured images using overlap mode. Once the UAV the target altitude tolerance (±15 m) below the target altitude, the Altum PT started capturing tracking forward movements to comply with the overlap percentage specified. For this study, the overlap percentage was set to 75%, front and back and side to side, which was found to provide the highest-quality image.

3.2. 2-Return LIDAR Sensor

The LiDAR sensor used herein was the R3Pro V2 by Rock Robotics; it is a lightweight (1.260 kg), two-return LiDAR (Figure 7) that obtains 1.28 million points/second. It is a class 1 laser of 905 nm wavelength. The LiDAR operation range is between −10 °C and 50 °C, with a reported accuracy of ±0.03 m in both horizontal and vertical direction by the manufacturer [38]. This two-return LiDAR has advantage over the multi-return LiDAR as it is less expensive (about 30% or less). It is also considered low-cost at approximately 30%, or less of the cost of a five-spectra LiDAR sensor and requires less data processing cost [39]. The LiDAR is accompanied by a 26 MP camera, which can take RGB images at a rate of two images per second with a pixel resolution of 0.023 m at a ground sampling distance (GSD) of 100 m. The LiDAR gets its power from the PRISM Lite UAV batteries via the Skyport mount.



Figure 7. Image of the LiDAR sensor.

3.3. Data Collection and Flights

UAV flights were made during peak stage of recent floods (Flood), during spring runoff (High), at near bankfull conditions (Near Bankfull), and during baseflow leaf-off conditions (Low) as presented in Table 2.

Table 2. UAV Flight Details.

Flight Area	Sensors	Flight Date (Time)-Season	River Flow
Blacksmith Fork reach	Altum-PT camera	5 May 2023 (3:00 P.M. to 4:06 P.M.)-Spring	Near Bankfull
	LiDAR sensor	3 May 2024 (9:12 A.M.–9:29 P.M.)-Spring	High
		22 November 2024 (14:43 A.M.–14:58 P.M.)-Fall	Low
Logan River reach	Altum-PT camera	24 May 2023 (10:33 A.M. to 2:54 P.M.)-Spring	Flood
	LiDAR sensor	14 May 2024 (10:37 A.M.–14:42 P.M.)-Spring	High
		22 November 2024 (09:58 A.M.–13:47 P.M.)-Fall	Low

For both UAV payloads (multispectral camera and LiDAR sensor), mission parameters (flight altitude, speed, and flight-line layout) were defined in the flight-planning software (Mission Planner v1.3.83) and uploaded to the UAV. Missions were flown autonomously, with the operator monitoring the aircraft and retaining the ability to assume manual control if needed.

No in-flight calibration was required for the multispectral camera. In contrast, the LiDAR sensor required a calibration procedure before and after each mission. After launch, and once a suitable flight altitude was reached, the UAV was flown forward in a straight line at full speed for 5 s, followed by a figure-eight maneuver prior to initiating the automated mission. After mission completion, a final calibration pass was performed by flying at full speed for 5 s.

The multispectral sensor (Figure 5a) was flown at 200 m above ground level (AGL) at a flight speed of 15 m/s. Flights were performed under clear, sunny conditions near optimal illumination to maximize image quality. Ground control points (GCPs) could not be deployed for the multispectral survey of Logan River flooding (24 May 2023) due to limited ability to anticipate the event. GCPs were also not deployed for the multispectral survey of near-bankfull flow conditions (5 May 2023) in the Blacksmith Fork River reach. As described in Section 3.4.3, multispectral accuracy was assessed using control points derived from the 2016 LiDAR dataset provided by the Utah Geospatial Resource Center (UGRC) [40].

The LiDAR sensor (Figure 5c) was flown at 50 m AGL at a flight speed of 5 m/s. The base station (Figure 5b) was positioned near the center of the river reach; after setup, it required no active operation, although one field team member remained onsite to ensure it was not disturbed. LiDAR surveys were performed twice: (1) during high-density vegetation conditions (spring 2024 during snowmelt-driven runoff) and (2) during leaf-off conditions (late fall 2024). No GCPs were deployed during LiDAR flights for direct accuracy assessment. Instead, LiDAR accuracy was independently verified using Propeller AeroPoints GCPs [41] collected during Fall 2024 cross-section surveys of the Logan and Blacksmith Fork rivers (Section 3.4.4).

3.4. Post Processing

This research did not develop any new post-processing techniques or methodology but used existing techniques as noted herein. Data obtained with the multi-spectral camera and LiDAR sensor were post-processed as summarized in Figure 8 via a workstation with 3.7 GHz AMD Ryzen 959000X 12-core processor, 128 GB RAM, and 64 GB NVIDIA GeFORCE RTX 3090 Ti GPU. Post-processing took approximately 3 days to generate the orthomosaic from the multi-spectral camera for a 1.5 km reach of the Blacksmith Fork River, whereas the Digital Surface Model (DSM) and Digital Terrain Mode (DTM) generation from the LiDAR sensor for the same reach took approximately 2.8 h.

3.4.1. Post Processing of the Multi-Spectral Sensor Data

Post-processing of the multispectral imagery followed the workflow shown in Figure 8a and was completed using Agisoft Metashape Professional (v2.2.0) and ArcGIS Pro v3.3. No post-processed kinematics (PPK) correction was applied to the imagery because base station was not used. Raw images were first imported into Metashape, and the panchromatic band (B3) was selected as the primary channel. Reflectance panel images were radiometrically calibrated, after which photos were aligned, and poor-quality tie points were removed to improve the reconstruction. Ground control points (GCPs) were then added and the project coordinate system was assigned to georeference the dataset. A dense point cloud was generated and cleaned, and DSM and multispectral orthomosaic were produced. Pansharpening was subsequently applied to increase spatial detail in the multispectral bands using the panchromatic band using the following relations where *B1* = Blue band, *B2* = Green band, *B3* = Panchromatic band, *B4* = Red band, *B5* = Red-edge band, *B6* = NIR band, and [42]:

$$\text{Pansharpened (Blue)} = B1 \times (B3/(0.2B1 + 0.2B2 + 0.2B4 + 0.2B5 + 0.2B6)) \quad (1)$$

$$\text{Pansharpened (Green)} = B2 \times (B3/(0.2B1 + 0.2B2 + 0.2B4 + 0.2B5 + 0.2B6)) \quad (2)$$

$$\text{Pansharpened (Red)} = B4 \times (B3/(0.2B1 + 0.2B2 + 0.2B4 + 0.2B5 + 0.2B6)) \quad (3)$$

$$\text{Pansharpened (Red edge)} = B5 \times (B3/(0.2B1 + 0.2B2 + 0.2B4 + 0.2B5 + 0.2B6)) \quad (4)$$

$$\text{Pansharpened (NIR)} = B6 \times (B3/(0.2B1 + 0.2B2 + 0.2B4 + 0.2B5 + 0.2B6)) \quad (5)$$

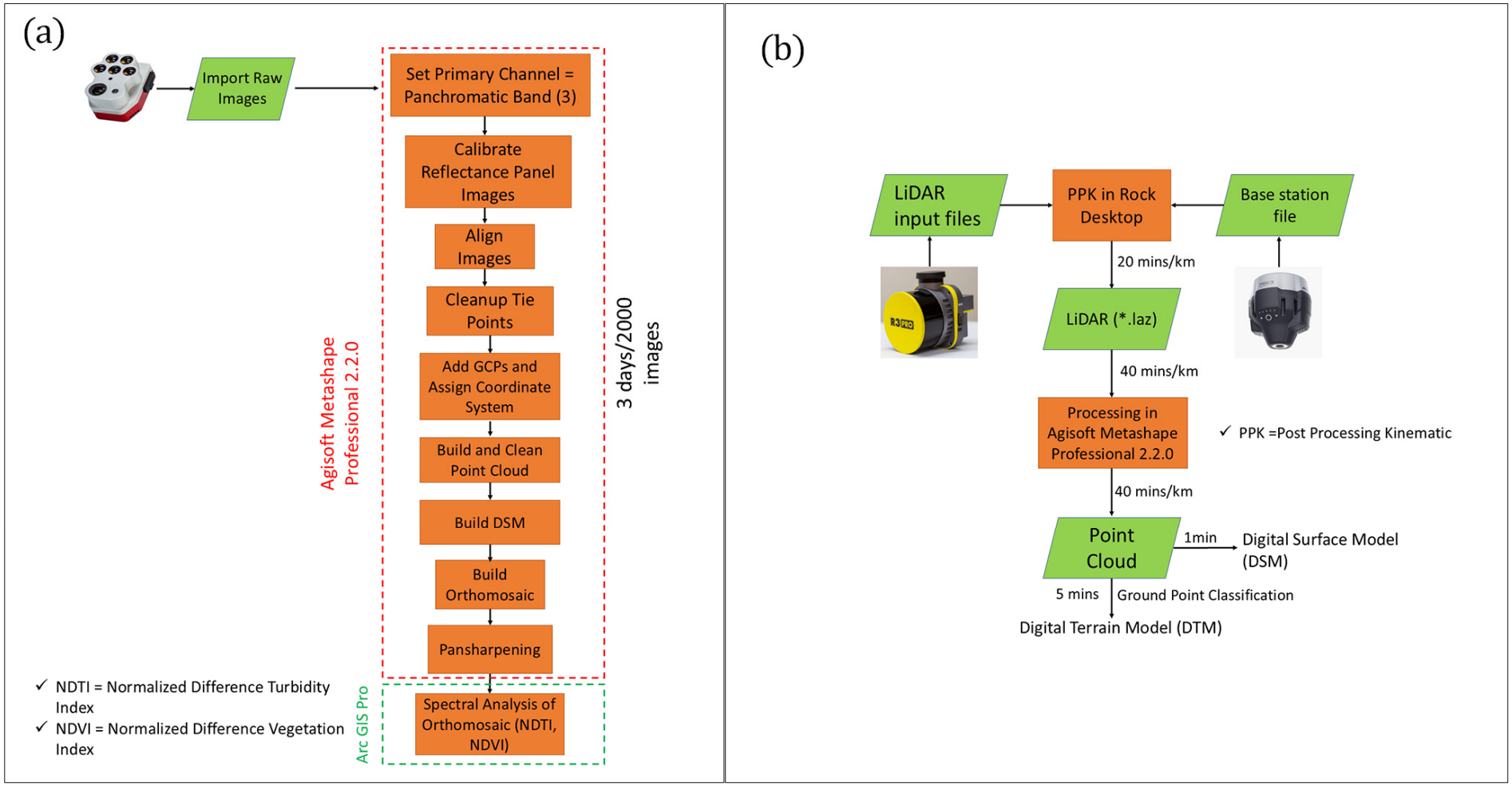


Figure 8. Data processing steps and software used: (**a**) Multi-spectra camera, and (**b**) LiDAR sensor.

If reflectance output was required, the pan-sharpened values were converted from scaled integer storage to reflectance by dividing above equations by 32,768.

Pansharpening was not applied to the thermal band (B7), as the thermal imagery has a different native spatial resolution and sharpening with the panchromatic band would not represent true thermal spatial detail. Thermal values were converted to degrees Celsius as:

$$B7 \text{ (degree Celsius)} = (B7/100) - 273.15 \quad (6)$$

where $B7$ = Thermal band.

Finally, the pansharpened orthomosaic was imported into ArcGIS Pro for spectral analysis. Raster calculator was used to compute the Normalized Difference Turbidity Index (NDTI) and Normalized Difference Vegetation Index (NDVI) [42]:

$$NDTI = \frac{B4 - B2}{B4 + B2} \quad (7)$$

$$NDVI = \frac{B6 - B4}{B6 + B4} \quad (8)$$

3.4.2. Post-Processing of the LiDAR Data

Post-processing of the LiDAR data followed the workflow shown in Figure 8b was completed using the LiDAR manufacturer's software (Rock Desktop v1.13.12) and Agisoft Metashape Professional (v2.2.0). Camera images collected during the flight were not used in the LiDAR processing.

First, Post-Processing Kinematic (PPK) was performed in Rock Desktop. In this step, the LiDAR system logs, and GNSS observations from the RS3 Reach EMLID base station were combined with the LiDAR's IMU measurements to improve the trajectory and georeferencing. The output was exported as a georeferenced LiDAR point cloud in *.laz format.

Second, the *.laz file was imported into Agisoft Metashape for terrain product generation. A Digital Surface Model (DSM) was generated directly from the LiDAR point cloud. To generate a Digital Terrain Model (DTM), Metashape's default ground-point classification tool was used to identify bare-earth points, and the DTM was produced using the classified ground (bare-earth) point cloud. The ground-point classification parameters are shown in Table 3.

Table 3. Ground point classification parameters.

SN	Parameters	Values
1	Max angle (°)	10
2	Max terrain slope (deg)	90
3	Max distance (m)	1
4	Cell size (m)	10

3.4.3. Spatial Resolution and Accuracy of the Multi-Spectral Sensor Data

The multispectral UAV flights over the Blacksmith Fork and Logan River reaches were conducted at an altitude of 200 m and a speed of 15 m/s. The initial ground sampling distance (pixel size) of the multispectral/RGB orthomosaic was 0.0872 m, while the thermal imagery had a native pixel size of 1.32 m. The pansharpening of the multi-spectral orthomosaic resulted in a pixel size of 0.0432 m. The thermal band was not pan-sharpened; instead, it was resampled from 1.32 m to 0.0432 m so that all outputs had the same pixel size for mapping and band calculations.

Because the flood events could not be anticipated in advance (5 May 2023, at Blacksmith Fork and 24 May 2023, at Logan River), field-surveyed GCPs were not collected during the flights. Therefore, ground-control points were derived from the 2016 LiDAR dataset and used in Metashape for georeferencing and accuracy evaluation after alignment. The project coordinate system assigned was NAD83(2011)/UTM zone 12N + NAVD88 Geoid 12B. For the Blacksmith Fork reach, 21 GCPs were used, with RMSE values of 0.0034 m (Easting), 0.0110 m (Northing), and 0.00269 (Elevation). For the Logan River reach, 41 GCPs were used, with RMSE values of 0.0172 m (Easting), 0.0109 m (Northing), and 0.00356 m (Elevation).

3.4.4. Spatial Resolution and Accuracy of the LiDAR Terrain Data

The LiDAR sensor produced a point cloud density of approximately 350 points/m^2 when flown at a height of 50 m and a speed of 5 m/s. This density was sufficient to generate both a Digital Surface Model (DSM) and a Digital Terrain Model (DTM) at a 0.05 m spatial resolution.

An accuracy assessment (Figure 9) was performed for the LiDAR terrain data collected at Blacksmith Fork on 22 November 2024 (14:43–14:58), and at the Logan River on 14 May 2024 (10:37–14:42). The LiDAR elevations were compared against independent check points from Propeller AeroPoints, which provide reported positional accuracies of 0.01–0.03 m in the x, y, and z directions. These AeroPoints were collected during cross-sectional survey work in Fall 2024, and the comparison was carried out in ArcGIS Pro in the coordinate system WGS 84/UTM Zone 12N + ellipsoidal height. The accuracy assessment was not repeated for the Blacksmith Fork flight on 3 May 2024 (09:12–09:29), and the Logan River flight on 22 November 2024 (09:58–13:47), because the base station location was kept the same.

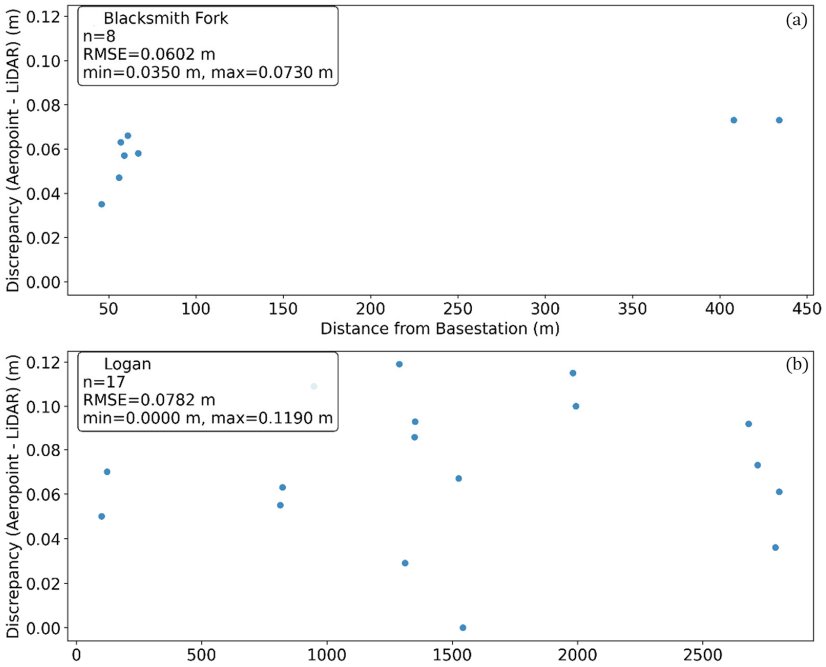


Figure 9. Discrepancy in the elevation difference between independent aeropoint and LiDAR Point in the two studied reaches: (**a**) Blacksmith Fork River Reach and (**b**) Logan River Reach.

For Blacksmith Fork, eight independent check points (n = 8) were used for the accuracy. The results (Figure 9a) show an RMSE of 0.0602 m, which means the LiDAR elevations differed from the AeroPoints by about 6 cm on average. The discrepancies were consistent, ranging from a minimum of 0.0350 m (3.5 cm) to a maximum of 0.0730 m (7.3 cm).

For the Logan River, 17 independent check points (n = 17) were used for the accuracy assessment. The RMSE was 0.0782 m, meaning the LiDAR and AeroPoint elevations differed by about 8 cm on average. The discrepancies covered a wider range than Blacksmith Fork, from 0.0000 m (near perfect match at one point) up to 0.1190 m (11.9 cm). This wider range shows that the error varies more from location to location along the Logan River corridor.

When examining error as a function of distance from the base station, Blacksmith Fork does not show a clear increase in discrepancy with distance. Points close to the base station (about 50–70 m) and points farther away (about 410–440 m) fall within a similar discrepancy range. For the Logan River, the check points span much larger distances (up to 2.8 km), but the discrepancies remain mixed across distances. Some moderate and larger discrepancies occur at mid-to-far distances, but there is no simple pattern showing that errors steadily grow as distance increases. Overall, based on these results, distance from the base station does not appear to be the main driver of the observed errors.

3.5. Integrated Methodological Workflow

To provide a clear overview of the full methodological framework, Figure 10 summarizes the sequence of study area and sensor selection, flight planning and UAV data collection, data post-processing, spatial resolution and accuracy assessment, geospatial datasets, results, and interpretation, and, finally, discussion, limitation, and future work.

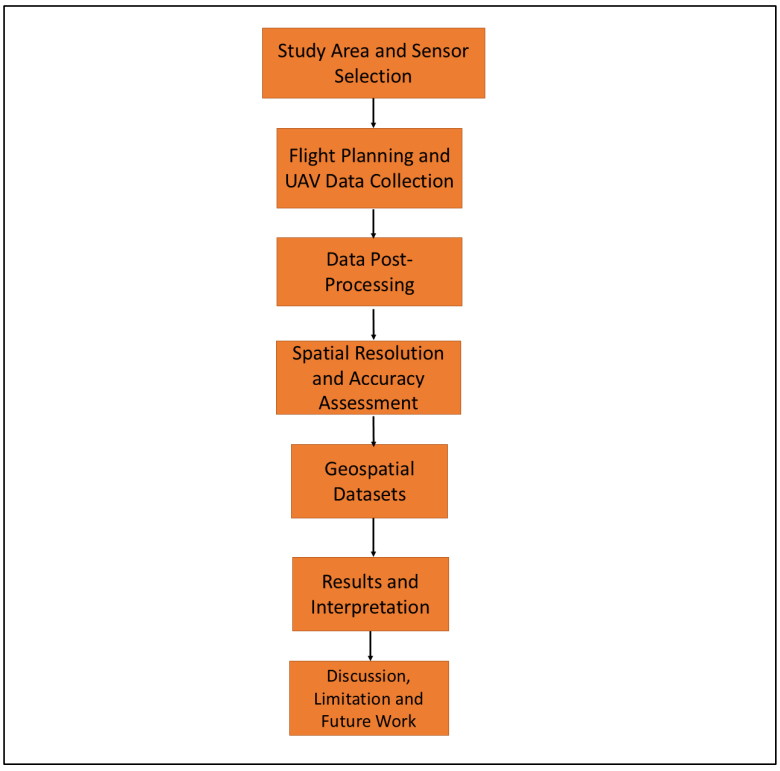


Figure 10. Integrated methodological workflow for this research study.

3.6. Summary of the Datasets

Table 4 summarizes the post-processed geospatial datasets for this study, which included UAV-based multispectral orthomosaic, UAV LiDAR DSM/DTM, vegetation and turbidity indices, flood extent maps, and river water levels. This table is included to clarify the source, temporal coverage, and spatial resolution/accuracy of the data. Details on these datasets and their interpretation are provided in Results (Section 4), which are discussed in Section 5.

Table 4. Summary of post-processed data in this study.

SN	River Corridor	Dataset/Product	Source	Temporal Scope	River Flow Condition	Resolution/Vertical Accuracy
1	Blacksmith Fork	UAV multi-spectral orthomosaic	Altum-PT Camera	5 May 2023	Near Bankfull	0.0432 m
2	Blacksmith Fork	LiDAR DSM/DTM	LiDAR sensor	3 May 2024	High	0.05 m/0.0602 m
3	Blacksmith Fork	LiDAR DSM/DTM	LiDAR sensor	22 November 2024	Low	0.05 m/0.0602 m
4	Blacksmith Fork	DEM of Difference (DODs)	LiDAR sensor	3 May 2024–22 November 2024	High–Low	0.05 m/0.078 m
6	Logan	UAV multi-spectral orthomosaic	Altum-PT Camera	24 May 2023	High	0.0432 m
7	Logan	Thermal orthomosaic	Altum-PT Camera	24 May 2023	High	0.0432 resampled from 1.32 m
8	Logan	Normalized Difference Turbidity Index (NDTI)	Altum-PT Camera	24 May 2023	High	0.0432 m
9	Logan	Normalized Difference Vegetation Index (NDTI)	Altum-PT Camera	24 May 2023	High	0.0432 m
10	Logan	LiDAR DSM/DTM	LiDAR sensor	14 May 2024	High	0.05 m/0.078 m
11	Logan	LiDAR DSM/DTM	LiDAR sensor	22 November 2024	Low	0.05 m/0.078 m
12	Logan	Flood Extent/Water Level	Altum-PT Camera/LiDAR Sensor	24 May 2023–22 November 2024	High–Low	-

4. Results

4.1. River Corridor Features Using Multi-Spectral Orthomosaic

River corridor features, both natural and anthropogenic, play a crucial role in controlling the hydrological, ecological, and morpho-dynamic regimes of a river. Changes in these regimes can significantly impact conservation efforts and the overall health of the river. With the multi-spectral imagery and resulting orthomosaic, we observed different natural and man-made features in the corridors of Blacksmith Fork and Logan River reach using the AgEagle Altum-PT camera.

In the Blacksmith Fork (Figure 11a), several features were clearly identifiable, including a fall structure (Figure 11b), a bridge and intake structure (Figure 11c), outer bank protection (Figure 11d), and wooden debris (Figure 11e). The high-resolution RGB orthomosaic (0.0432 m) supported estimating the approximate planar dimensions with an uncertainty of 0.0432 m. For instance, the intake opening measured 4.2 m, the maximum boulder size used for bank protection was 1.2 m, the total length of the protection structure was 56 m, and the longest individual stem of the wooden debris measured 6 m.

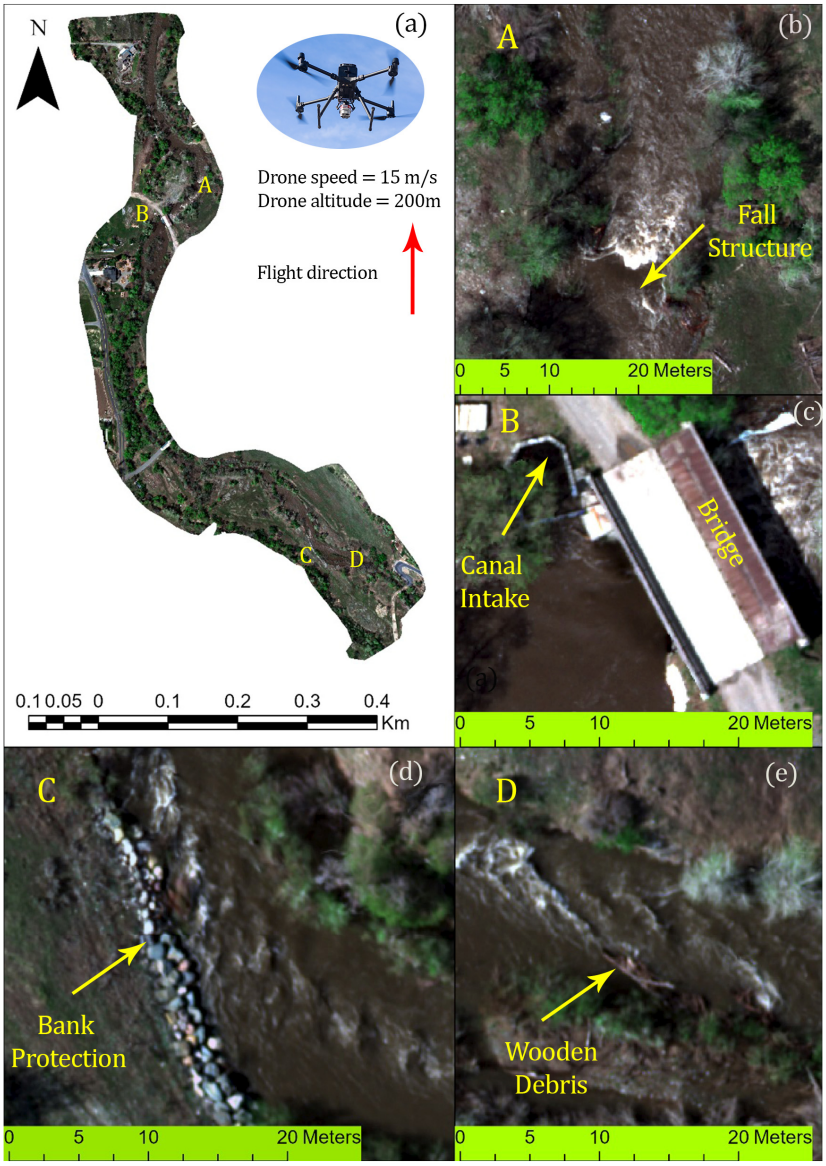


Figure 11. River corridor features in the Blacksmith Fork (**a**) seen through multi-spectral orthomosaic. (**b**) Fall structure, (**c**) Canal intake, (**d**) Outer bank protection, and (**e**) Wooden debris.

Along the Logan River (Figure 12a), a diverse array of corridor features was captured in the RGB orthomosaic, including an oxbow lake (Figure 12b), micro-topographies in the floodplain (Figure 12c), mobile housing located near the maximum flood inundation extent (Figure 12d), and a farmhouse with active agricultural practices (Figure 12e).

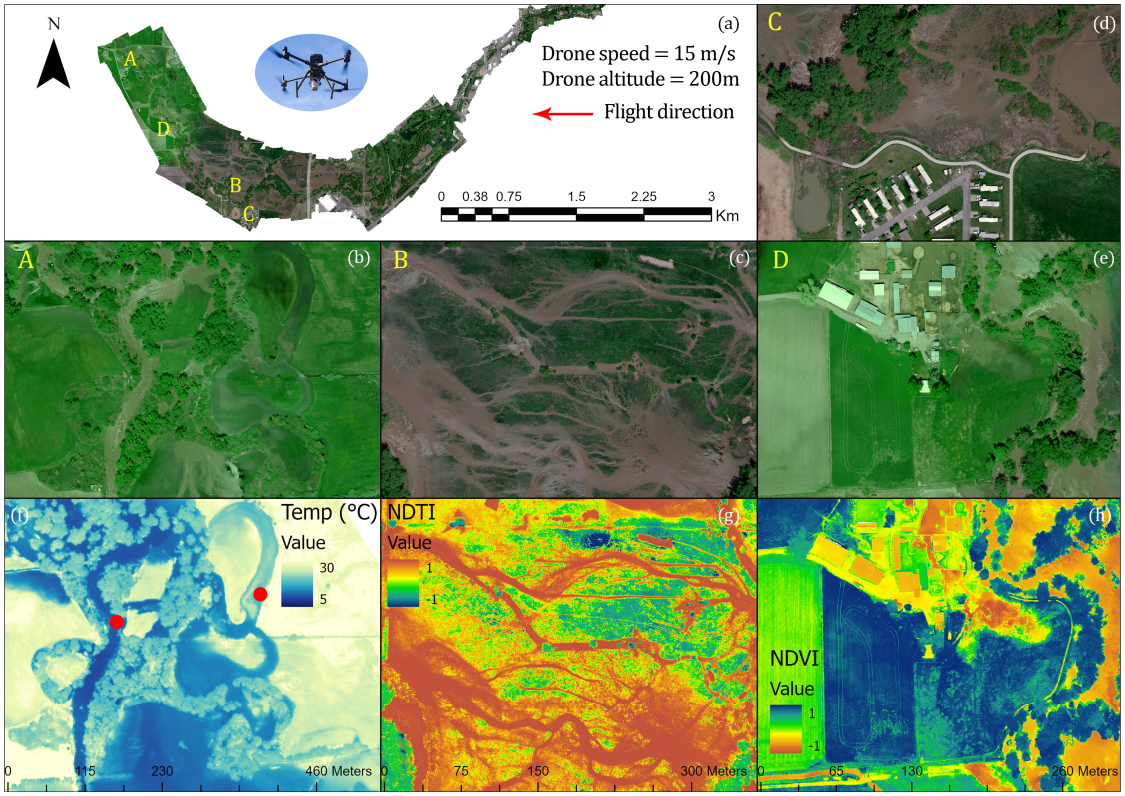


Figure 12. River corridor features in the Logan River seen through multi-spectral orthomosaic. (**a**) overview of river reach with four locations identified in yellow (**b**) Oxbow lake, (**c**) Micro-topographies in flood plain, (**d**) Mobile housing near flood plain, (**e**) Farmhouse with agriculture outbuildings, (**f**) Water surface temperature, (**g**) Normalized Difference Turbidity Index (NDTI) of the flood water, and (**h**) Normalized Difference Vegetation Index (NDVI) of vegetation.

The AgEagle Altum-PT camera, equipped with thermal sensor (Table 1), provided an opportunity to assess temperature variations within the main channel and the oxbow lake (Figure 12f). At a designated point (marked with a red dot in Figure 12f), the surface temperature difference between the main channel and the oxbow lake was measured at 7 °C. Furthermore, via Equations (7) and (8), we calculated two key indices—the Normalized Difference Turbidity Index (NDTI) and the Normalized Difference Vegetation Index (NDVI)—to analyze turbidity levels in the floodplain water and classify vegetation types near farmland. The NDTI values range from −1 to 1, with positive values indicating turbidity in the water (Figure 12g), whereas NDVI values also range from −1 to 1, with positive values signifying the presence of different vegetation classes within the river corridor (Figure 12h).

4.2. River Corridor Features Using LiDAR Digital Terrain Model

LiDAR flights were made during the Spring 2024 and Fall 2024 in both the Blacksmith Fork and Logan River, as shown in Table 2. A Digital Terrain Model (DTM) was produced for the Blacksmith Fork corridor for both seasons, as shown in Figure 13, at a resolution of 0.05 m and vertical accuracy of 0.060 m (RMSE). A temporal change analysis was done to see the changes in the river corridor due to natural or man-made interventions for which a

DEM of Difference (DOD) was produced (Figure 13d). The DOD well-represented the river channel and two irrigation canals in the corridor. Spring and Fall periods (Figure 13e,f) revealed significant changes in the riverbanks primarily caused by a new structure at the upstream face of the bridge that elevated the water surface and was a sediment barrier. In addition to these changes, water surface elevation was obtained from the LiDAR DTM. For example, the water surface elevation at the designated point (red dot) in Figure 13e,f was 1405.26 m in Spring and 1404.74 m in Fall. DSM and DTM were also produced for the Logan River corridor at a resolution of 0.05 m, with vertical accuracy of 0.078 m (RMSE). The DTM developed showed a remarkable development in the existing flood plain area as shown in Figure 14. A levee was first constructed in Spring of 2024 (Figure 14d) for a potential residential area development in the floodplain. This levee also included channel modification at some points along the original Logan River channel. Then roads and ponds were developed in the Fall of 2024 (Figure 14f). The DTM from the LiDAR shows that the levee was 1–3 m above the original floodplain level.

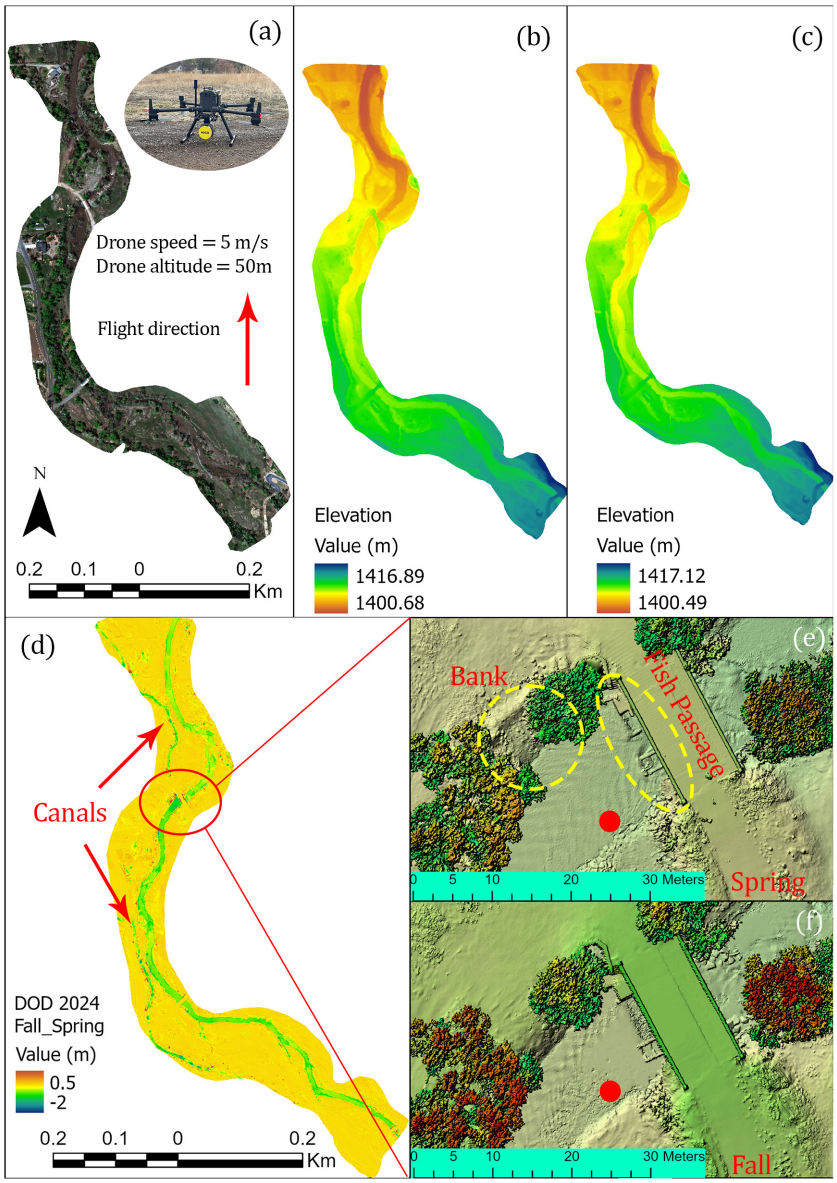


Figure 13. Digital Terrain Models of the Blacksmith Fork River corridor and temporal changes seen in the span of 6 months, 2024. (**a**) overview of river reach and UAV, (**b**) DTM for Spring 2024, (**c**) DTM for Fall 2024, (**d**) DEM of Difference (DOD) of Fall and Spring DTM with (**e**) DEM for Spring and (**f**) DEM for Fall.

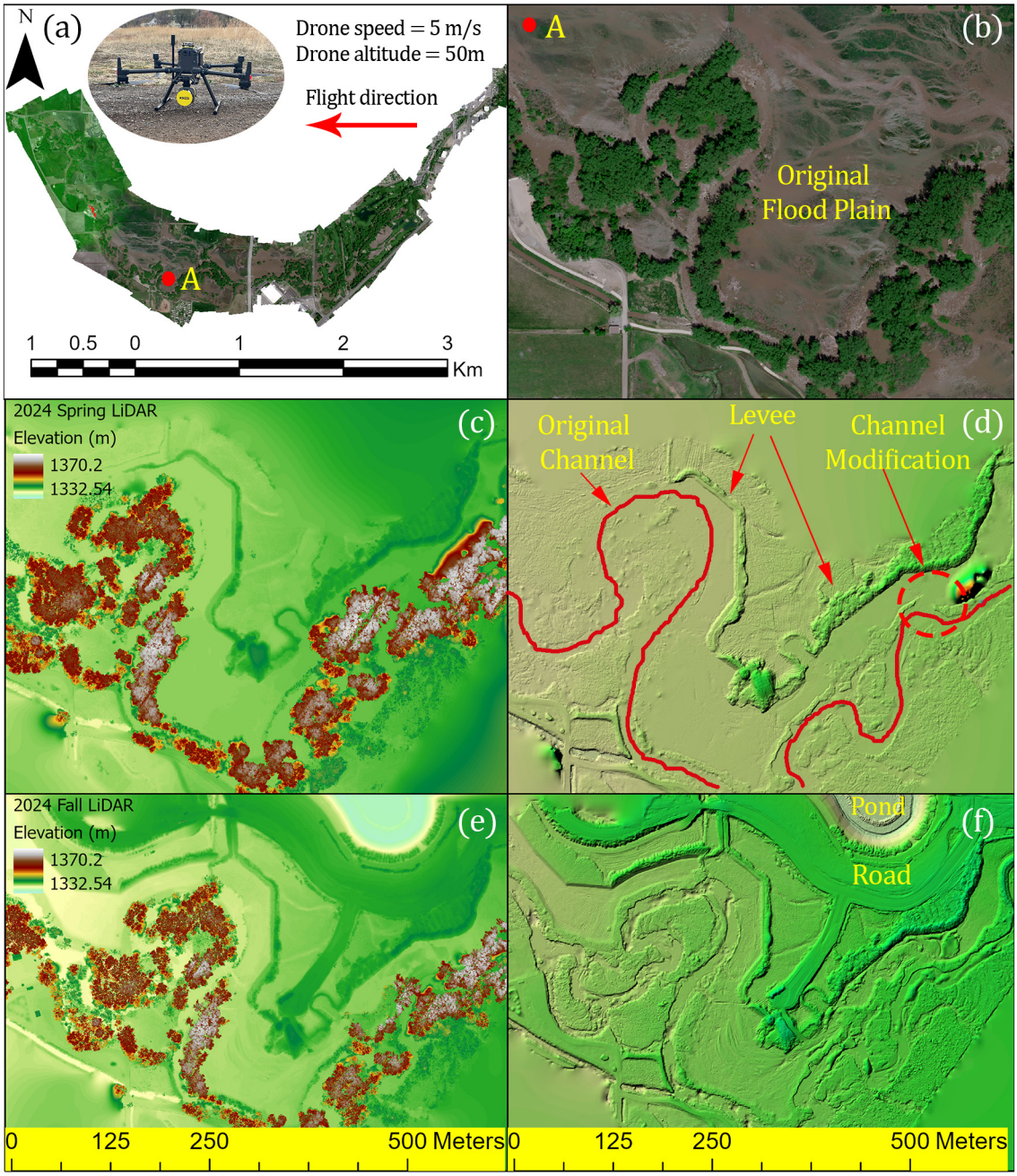


Figure 14. Flood plain developmental activities (Hazard Creep) in the span of 6 months in the Logan River with (**a**) overview of reach and select location, (**b**) original flood plain at start of 6 months, (**c**) Spring 2024 LiDAR, (**d**) noted channel modification and original alignment (**e**) Fall 2024 LiDAR with noted changes due to urbanization, and (**f**) Fall DEM with Pond and Road.

4.3. Additional Information Combining Multi-Spectral Imagery and LiDAR

Demarcation of maximum flood extent to the level of individual building was also possible using the multi-spectral orthomosaic, as shown in Figure 15. These demarcations are important for numerical model calibration and flood insurance. Also, when the maximum flood extent in 2023 Spring flood was combined with the LiDAR DEM for 2024 Fall, their corresponding water level was also obtained, as shown in Figure 15b.

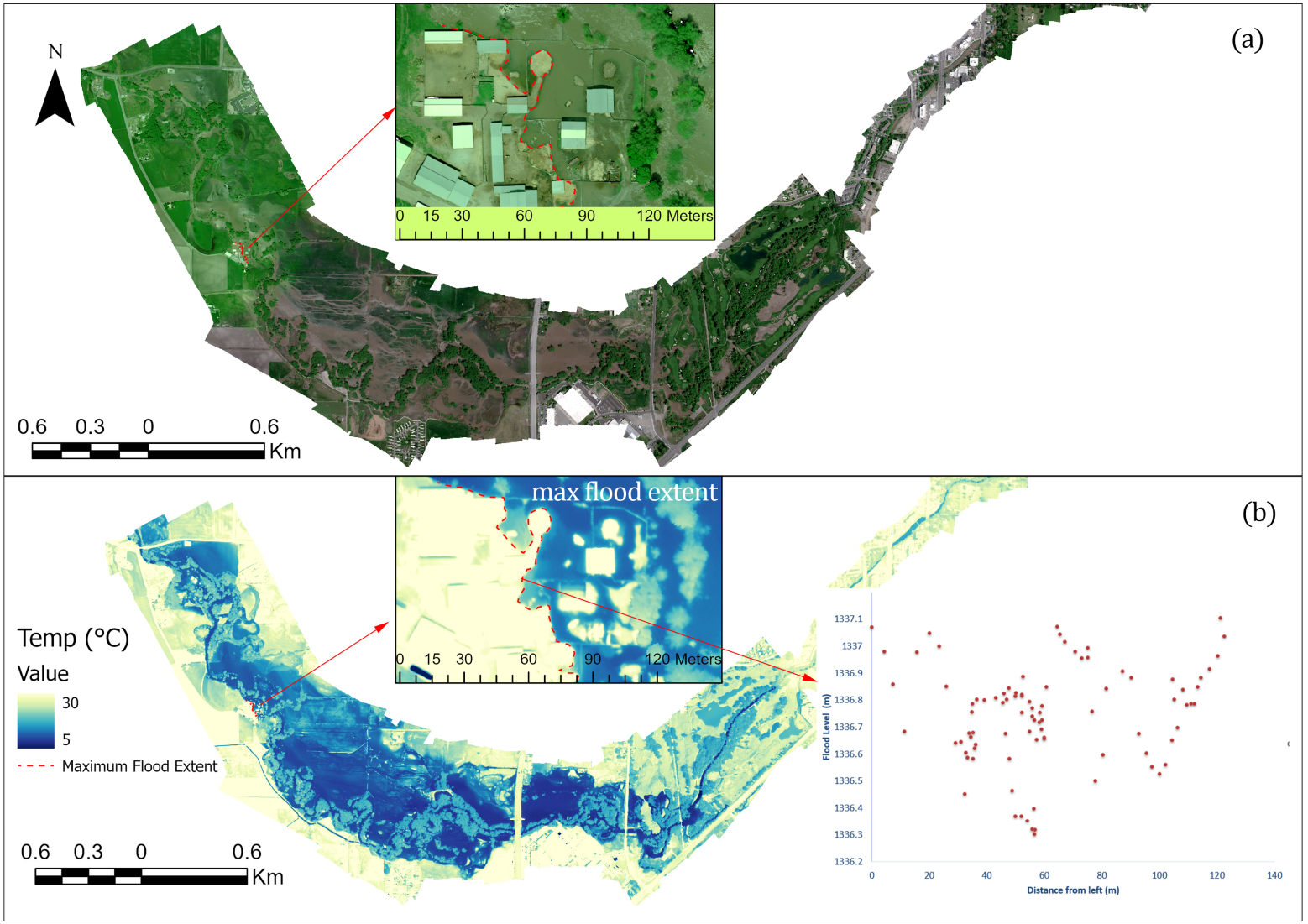


Figure 15. Maximum flood extent at the scale of individual housing and their corresponding water levels. (**a**) RGB orthomosaic, (**b**) Thermal orthomosaic. The thermal orthomosaic shows the flood extent more clearly than the RGB orthomosaic. The maximum flood extent and the corresponding flood levels are important data for numerical model calibration and flood insurance.

5. Discussion

5.1. River Corridor Remote Sensing Observations and Their Implications

The combination of multi-spectral and LiDAR sensors used in this study provided detailed and diverse data via multiple UAV flights, providing insights into specific flood events and how the rivers were being modified over time (and corresponding responses). These data have significant implications for reach-scale hydraulic modeling, catchment hydrology, river corridor ecology, floodplain conditions, and real-time monitoring of floods, as highlighted via the Blacksmith Fork (Table 5) and Logan River (Table 6). Practical applications also include high-resolution flood data, obtaining geospatial data of river corridors to support the setting of flood insurance rates, identification of structures such as critical infrastructure and residences for hazard estimates, performing two-dimensional hydraulic flood modeling of observed and hypothetical floods, and supporting local municipalities with floodplain management decisions or stream restoration efforts, including post-project or post-construction monitoring.

Table 5. Observed features in the corridor of Blacksmith River using multi-spectral and LiDAR sensors.

River Stretch	Sensors	Corridor Features		Reference in this Article	General Hydrological, Ecological and Morpho-Dynamic Impact at Reach Scale
		Main Channel	Flood Plain		
Blacksmith Fork	Multi-Spectral (AgEagle ALTUM-PT)	Fall Structure		Figure 11b	Decrease in channel bed slope, fish movement, local scour
		Intake structure and bridge		Figure 11c	Changes in river flow, changes in approach flow upstream of these structures, local scour near bridge abutment
		Bank protection		Figure 11d	Bank stability, local changes in flow
		Wooden Debris		Figure 11e	Sediment deposition, fish habitat, flooding
	LiDAR (R3 Pro Rock Robotics)	Temporal riverbank changes		Figure 13e-Spring and Figure 13f-Fall	Channel migration, increase in sediment transport in river, water quality
		Temporal variations in Water Level		Figure 13e-Spring and Figure 13f-Fall	Fish habitat and bank vegetations
		Temporal changes in fish passage structures		Figure 13e-Spring and Figure 13f-Fall	Approach flow, fish movement, flooding
		Canal Alignment		Figure 13d	Irrigation area, flood dynamics

Table 6. Observed features in the corridor of the Logan River using multi-spectral and LiDAR sensors.

River Stretch	Sensors	Corridor Features	Reference in this Article	General Hydrological, Ecological and Morpho-Dynamic Impact at Reach Scale
Logan	Multi-Spectral (AgEagle ALTUM-PT)	Oxbow Lake	Figure 12b	Fish habitat, flood dynamics
		Micro topographies	Figure 12c	Flood dynamics
		Mobile Housing	Figure 12d	Flood dynamics
		Farmhouse with Agricultural Practice	Figure 12e	Vegetation in floodplain, nutrients in river
		Water Temperature Index	Figure 12f	Water quality, fish habitat
		Water Turbidity Index	Figure 12g	Water quality, fish habitat
		Vegetation Index	Figure 12h	Vegetation classes
	LiDAR (R3 Pro Rock Robotics)	Progressive development in Floodplain (Levee, roads)	Figure 14d Figure 14f	Future flood dynamics
		Channel Modifications	Figure 14d	Future flood dynamics, bank erosion, changes in flow
		Maximum flood extent at the scale of individual building	Figure 15a, Figure 15b	Flood Insurance, flood dynamics
		Maximum flood extent and its level	Figure 15b	Flood dynamics

For example, in the Logan River, an index on turbidity was derived using the multi-spectral sensor (Figure 12g), while details on progressive floodplain development, such as floodplain, levee, and channel modifications (Figure 14), were captured primarily by the LiDAR sensor and its 3D mapping capabilities. The maximum flood extent and corresponding water levels (Figure 15) were rapidly and safely acquired through a combination of multi-spectral orthomosaic and LiDAR data. Similarly, changes in channel bank, a fish passage structure, and seasonal water levels in Blacksmith Fork during two different periods in 2024 were clearly mapped using LiDAR (Figure 13).

This study also confirmed that regular urbanization activities as populations increase can have a large impact on a river corridor within a short period of time (approx. 6 months), as shown by the changes in the bank and removal of fish passage structure in the Blacksmith Fork River (Figure 13) and by the floodplain developmental activities in the Logan River (Figure 14). Utilizing these remote sensing techniques could inform municipalities and other stakeholders as projects are considered and provide valuable and up-to-date data for river management practices. Perhaps the most serious consequences are linked to moderate and severe flooding impacts, as observed in Missouri River Flooding (14–31 March 2019), Mississippi River Flooding (March–July 2019), and Arkansas River Flooding (20 May–14 June 2019) [43], which includes an increasing challenge of heavy precipitation following forest fires as observed in Montecito and Carpinteria, California [44] and Grizzly Creek Fire, Colorado [45]. Leveraging these data could decrease uncertainties with flood mapping and hazard identification and facilitate efforts to update or keep current existing flood maps.

This study has certain limitations related to the post-processing and geometric correction of the multispectral orthomosaic. A base station, such as RTK or PPK, was not used to correct image positions during flight to increase accuracy beyond what the system provides. In addition, the ground control points and accuracy assessment were derived from the 2016 LiDAR dataset rather than from independently surveyed field control points

from a licensed surveyor. This approach reflects using any available geospatial data such as from past surveys or structure survey markers or coarser LiDAR flights. The 2016 LiDAR dataset used herein, however, is a high-quality QL1 product, with 0.5 m of DEM products and a planned vertical RMSEz of $\leq$10 cm. The LiDAR report also provides DEM vertical accuracy values of NVA = 0.0668 m and VVA = 0.2357 m, where NVA represents accuracy in non-vegetated/open areas and VVA represents accuracy in vegetated areas. However, the report does not clearly provide a final horizontal accuracy value for the delivered DEM. Therefore, any positional uncertainty in the 2016 LiDAR dataset may have propagated into the multispectral orthomosaic and influenced the reported accuracy metrics. As a result, the orthomosaic should be interpreted as relative mapping products rather than survey-grade products. They are suitable for floodplain-scale interpretation, flood extent mapping, river corridor feature identification, vegetation and turbidity pattern analysis, and building-scale visualization of flood exposure. Future work could expand upon this research by using base-station-enabled positioning during drone flights, such as RTK or PPK, and independently surveyed GCPs and checkpoints for both georeferencing and accuracy assessment. This would allow for a more complete quantification of horizontal and vertical errors and improve confidence in using multispectral orthomosaic for detailed flood and terrain-related applications.

5.2. Validation of the Water Quality Indices

This study could not validate different water-quality indices such as NDTI and NDVI due to lack of availability of the field data for flooding conditions. The validation of this data would strengthen the research. These indices thus should be taken as exploratory indicators of turbidity and vegetation condition rather than calibrated quantitative estimates. Future monitoring should pair georeferenced turbidity measurements and vegetation survey plots with drone-derived NDTI and NDVI values and evaluate their relationships using correlation, regression, and error statistics, following established remote-sensing validation approaches described in [46,47].

5.3. Sensor Limitations

Both sensors have certain limitations. The multi-spectral sensor is sensitive to weather conditions, with optimal performance occurring under a clear blue sky. Cloud cover, shadows, haze, changing illumination, and water-surface glare may affect radiometric correction, orthomosaic quality, and the interpretation of derived indices such as NDVI and NDTI. Additionally, the altitude at which the multispectral sensor could be flown could be restricted due to local laws. For example, in the US, for any drone flights, 121 m of AGL requires authorization from the Federal Aviation Administration (FAA) [48]. Such restrictions can limit spatial coverage and may require additional flight lines for larger river corridors.

For the LiDAR sensor, the optimal flight altitude is 50 m AGL, and the speed must not exceed 5 m/s. At this altitude, a single flight can cover only 60 m of swath width. In cases where river corridors are wide, such as in large rivers, multiple overlapping flights may be necessary to ensure full coverage of the desired study area. Furthermore, the LiDAR signal may be absorbed by calm water, reducing the number of additional ground points captured. This may specifically create problems while producing the Digital Terrain Models. Other limitations with the LiDAR sensor used in this study were that it could not penetrate the water surface, requiring any such information to be measured with other techniques, such as green LiDAR, sonar, or a direct field survey.

5.4. Comparison with Previous Literature and Novelty of the Work

Previous studies have demonstrated the value of UAV-based remote sensing of river-corridors. Tomsett and Leyland [13] reviewed the increasing use of UAV-based remote sensing for river-corridors and highlighted the importance of high-resolution data for river morphology, vegetation, and floodplain analysis. Wienhold et al. [49] demonstrated that UAV-based multispectral imagery can be used for flood inundation and depth mapping during actual flood events. Similarly, Annis et al. [50] showed that UAV-derived DEMs can support small-scale flood hazard mapping, while Muhadi et al. [51] emphasized the broader importance of LiDAR-derived DEMs in flood applications because accurate terrain representation is critical for floodplain and water-level analysis. More recently, Tomsett and Leyland [52] combined repeat UAV laser scanning and multispectral imagery to examine eco-geomorphic feedback along a river corridor.

The present study builds on these previous efforts by integrating UAV-based multi-spectral imagery and UAV LiDAR for river-corridor assessment. Compared with studies focused mainly on flood extent/depth mapping or terrain-based flood modeling, this study presents wide array of data for hydrological, ecological, and morphological studies, with particular focus on a flood event in the Logar River. Therefore, the novelty of this study lies in its integrated multi-sensor framework for exploration of flood-impact and river-corridor assessment at river corridor scale. At the same time, the results should be interpreted with the limitations discussed above, particularly the need for stronger field validation, uncertainty analysis, and quantitative comparison with traditional measurements.

6. Conclusions

This study demonstrated the value of integrating UAV-based multi-spectral imagery and LiDAR data for high-resolution river corridors and flood assessment. The multispectral sensor provided spectral information useful for mapping flood extent, vegetation patterns, water-related surface conditions, and relative turbidity patterns, while the LiDAR sensor provided three-dimensional terrain and surface information needed to identify channel banks, levees, floodplain surfaces, built features, and seasonal water-level conditions. Together, these sensors provided complementary information that would be difficult to obtain from either sensor alone. These observations can support reach-scale hydraulic modeling, catchment hydrology, river corridor ecology, floodplain conditions, and real-time monitoring of floods.

This study also provides practical information on the cost of generated data products. For a river reach comparable to the Blacksmith Fork study reach, approximately 1.5 km in length, the flight and post-processing cost was approximately USD 2092 for the UAV-based multispectral survey and USD 1718 for the UAV-based LiDAR survey, excluding equipment purchase costs. These values indicate that UAV-based surveys can provide detailed local-scale flood and river corridor information at relatively low operational cost for river corridors.

However, this study has several limitations. The multispectral imagery was not corrected using RTK/PPK base-station positioning, and georeferencing and accuracy assessment relied on the 2016 LiDAR dataset rather than independently surveyed field GCPs. Field validation data were also not available during the flood events for several image-based observations and derived indices such as NDVI and NDTI. Therefore, the multi-spectral and integrated multi-spectral/LiDAR datasets should be interpreted as exploratory and relatively mapping output rather than fully validated or ground-controlled products. However, LiDAR datasets are free from such limitations as they were independently verified with ground control points. Future work should address these limitations by using RTK/PPK-supported multispectral image positioning, independently surveyed

GCPs and checkpoints, field-based validation of water levels and spectral indices, and formal uncertainty analysis.

This study also identified several operational limitations of the multispectral and LiDAR sensors. Multispectral imagery was sensitive to weather, illumination, shadows, haze, and water-surface glare, which may affect radiometric correction, orthomosaic quality, and indices such as NDVI and NDTI. Flight-altitude restrictions may also limit spatial coverage, especially for larger river corridors. The LiDAR sensor was limited by its required flight altitude, speed, and swath width, which may require multiple overlapping flights for wider river sections. In addition, reduced returns over calm water and the inability to penetrate the water surface limited its use for bathymetric mapping, requiring complementary methods such as green LiDAR, sonar, or direct field surveys.

Overall, this study shows that integrated UAV multispectral and LiDAR monitoring can provide a practical and flexible framework for documenting river corridor changes, flooding, and local floodplain conditions at a river corridor scale.

Author Contributions: Conceptualization: I.J. and B.M.C.; Methodology: I.J., I.G. and B.M.C.; Formal analysis and investigation I.J. and B.M.C.; Writing—original draft preparation: I.J.; Writing—review and editing: B.M.C. and I.G.; Funding acquisition: B.M.C.; Resources: B.M.C.; Supervision: B.M.C. All authors have read and agreed to the published version of the manuscript.

Funding: This study was funded by Utah State University and the Utah Water Research Laboratory.

Data Availability Statement: Data are available upon reasonable request to the corresponding author.

Acknowledgments: The authors thank the Utah Water Research Laboratory for support during this study.

Conflicts of Interest: The authors declare no conflicts of interest.

References

1. Moglia, M.; Cook, S.; Tapsuwan, S. Promoting Water Conservation: Where to from Here? *Water* **2018**, *10*, 1510. [CrossRef]
2. Parker, H.; Oates, N. *How Do Healthy Rivers Benefit Society. A Review of the Evidence*; ODI and WWF: London, UK, 2016.
3. Cooper, M.; Chakraborty, A.; Chakraborty, S. *Rivers and Society*; Routledge: London, UK, 2017; ISBN 9781315680088.
4. Tate, C.M.; Dennehy, K.F.; Luft, G. South Platte River; "Lifeline of a Region". 1999. Available online: https://pubs.usgs.gov/of/1999/0056/report.pdf (accessed on 10 February 2024).
5. Carlson, C.A.; Muth, R.T. The Colorado River: Lifeline of the American Southwest. *Can. Spec. Publ. Fish. Aquat. Sci.* **1989**, *106*, 220–239.
6. Wang, L.; Cui, S.; Li, Y.; Huang, H.; Manandhar, B.; Nitivattananon, V.; Fang, X.; Huang, W. A Review of the Flood Management: From Flood Control to Flood Resilience. *Heliyon* **2022**, *8*, e11763. [CrossRef] [PubMed]
7. Van Looy, K.; Tonkin, J.D.; Floury, M.; Leigh, C.; Soininen, J.; Larsen, S.; Heino, J.; LeRoy Poff, N.; Delong, M.; Jähnig, S.C.; et al. The Three Rs of River Ecosystem Resilience: Resources, Recruitment, and Refugia. *River Res. Appl.* **2019**, *35*, 107–120. [CrossRef]
8. Palmer, M.A.; Lettenmaier, D.P.; Poff, N.L.; Postel, S.L.; Richter, B.; Warner, R. Climate Change and River Ecosystems: Protection and Adaptation Options. *Environ. Manag.* **2009**, *44*, 1053–1068. [CrossRef] [PubMed]
9. de Bruijn, K.M. Resilience Indicators for Flood Risk Management Systems of Lowland Rivers. *Int. J. River Basin Manag.* **2004**, *2*, 199–210. [CrossRef]
10. Boon, P.J. Revisiting the Case for River Conservation. In *River Conservation and Management*; Wiley: Hoboken, NJ, USA, 2012; pp. 1–14.
11. Linke, S.; Pressey, R.L.; Bailey, R.C.; Norris, R.H. Management Options for River Conservation Planning: Condition and Conservation Re-visited. *Freshw. Biol.* **2007**, *52*, 918–938. [CrossRef]
12. Boon, P.J.; Davies, B.R.; Petts, G.E. Global Perspectives on River Conservation: Policy and Practice. *Environ. Pract.* **2001**, *3*, 190–191. [CrossRef]
13. Tomsett, C.; Leyland, J. Remote Sensing of River Corridors: A Review of Current Trends and Future Directions. *River Res. Appl.* **2019**, *35*, 779–803. [CrossRef]
14. Bizzi, S.; Demarchi, L.; Grabowski, R.C.; Weissteiner, C.J.; Van de Bund, W. The Use of Remote Sensing to Characterise Hydromorphological Properties of European Rivers. *Aquat. Sci.* **2016**, *78*, 57–70. [CrossRef]

15. Marcus, W.A.; Fonstad, M.A. Remote Sensing of Rivers: The Emergence of a Subdiscipline in the River Sciences. *Earth Surf. Process. Landf.* **2010**, *35*, 1867–1872. [CrossRef]
16. Smith, L.C. Satellite Remote Sensing of River Inundation Area, Stage, and Discharge: A Review. *Hydrol. Process.* **1997**, *11*, 1427–1439. [CrossRef]
17. Hilgert, S.; Sotiri, K.; Fuchs, S. Review of Methods of Sediment Detection in Reservoirs. *Int. J. Sediment Res.* **2023**, *39*, 28–43. [CrossRef]
18. Kostaschuk, R.; Best, J.; Villard, P.; Peakall, J.; Franklin, M. Measuring Flow Velocity and Sediment Transport with an Acoustic Doppler Current Profiler. *Geomorphology* **2005**, *68*, 25–37. [CrossRef]
19. Sabol, B.M.; Melton, R.E.; Robert, C.; Doering, P.; Haunert, K. Evaluation of a Digital Echo Sounder System for Detection of Submersed Aquatic Vegetation. *Estuaries* **2002**, *25*, 133–141. [CrossRef]
20. Leyland, J.; Hackney, C.R.; Darby, S.E.; Parsons, D.R.; Best, J.L.; Nicholas, A.P.; Aalto, R.; Lague, D. Extreme Flood-driven Fluvial Bank Erosion and Sediment Loads: Direct Process Measurements Using Integrated Mobile Laser Scanning (MLS) and Hydro-acoustic Techniques. *Earth Surf. Process. Landf.* **2017**, *42*, 334–346. [CrossRef]
21. Townsend, P.A.; Walsh, S.J. Modeling Floodplain Inundation Using an Integrated GIS with Radar and Optical Remote Sensing. *Geomorphology* **1998**, *21*, 295–312. [CrossRef]
22. Gilvear, D.; Bryant, R. Analysis of Aerial Photography and Other Remotely Sensed Data. In *Tools in Fluvial Geomorphology*; Wiley: Hoboken, NJ, USA, 2003; pp. 135–170.
23. Young, S.; Peschel, J.; Penny, G.; Thompson, S.; Srinivasan, V. Robot-Assisted Measurement for Hydrologic Understanding in Data Sparse Regions. *Water* **2017**, *9*, 494. [CrossRef]
24. Mader, D.; Blaskow, R.; Westfeld, P.; Maas, H.-G. UAV-Based Acquisition of 3D Point Cloud—A Comparison of a Low-Cost Laser Scanner and SFM-Tools. *Int. Arch. Photogramm. Remote Sens. Spat. Inf. Sci.* **2015**, *XL-3/W3*, 335–341. [CrossRef]
25. Legleiter, C.J. Remote Measurement of River Morphology via Fusion of LiDAR Topography and Spectrally Based Bathymetry. *Earth Surf. Process. Landf.* **2012**, *37*, 499–518. [CrossRef]
26. Fonstad, M.A.; Dietrich, J.T.; Courville, B.C.; Jensen, J.L.; Carbonneau, P.E. Topographic Structure from Motion: A New Development in Photogrammetric Measurement. *Earth Surf. Process. Landf.* **2013**, *38*, 421–430. [CrossRef]
27. Westoby, M.J.; Brasington, J.; Glasser, N.F.; Hambrey, M.J.; Reynolds, J.M. 'Structure-from-Motion' Photogrammetry: A Low-Cost, Effective Tool for Geoscience Applications. *Geomorphology* **2012**, *179*, 300–314. [CrossRef]
28. Detert, M.; Weitbrecht, V. A Low-Cost Airborne Velocimetry System: Proof of Concept. *J. Hydraul. Res.* **2015**, *53*, 532–539. [CrossRef]
29. Bolognesi, M.; Farina, G.; Alvisi, S.; Franchini, M.; Pellegrinelli, A.; Russo, P. Measurement of Surface Velocity in Open Channels Using a Lightweight Remotely Piloted Aircraft System. *Geomat. Nat. Hazards Risk* **2017**, *8*, 73–86. [CrossRef]
30. Legleiter, C.; Overstreet, B.; Kinzel, P. Sampling Strategies to Improve Passive Optical Remote Sensing of River Bathymetry. *Remote Sens.* **2018**, *10*, 935. [CrossRef]
31. Nex, F.; Rinaudo, F. LiDAR or Photogrammetry? Integration Is the Answer. *Ital. J. Remote Sens.* **2011**, *43*, 107–121. [CrossRef]
32. HydroServer | Site. Available online: https://lro.hydroserver.org/sites/191a4d08-a441-479f-9edf-2df745aace26 (accessed on 24 June 2025).
33. HydroServer | Site. Available online: https://lro.hydroserver.org/sites/ae623bc0-8cfa-476a-a3d5-f868ac2b33a7 (accessed on 24 June 2025).
34. Hydroserer. StreamStats. Available online: https://lro.hydroserver.org/sites/598b164e-a42f-435d-970d-3c78859d2799 (accessed on 24 June 2025).
35. Utah's Watershed Restoration Initiative. Blacksmith Fork Fish Passage and Habitat Restoration. 2023. Available online: https://wri.utah.gov/wri/reports/ProjectSummaryReport.html?id=6049 (accessed on 8 July 2026).
36. Utah Water Research Laboratory. *Logan River Restoration Conservation Action Plan*; Logan, 2016. Available online: https://uwrl.usu.edu/files/pdf/logan-river-observatory/2016-may-logan-river-restoration-conservation-action-plan.pdf (accessed on 8 July 2026).
37. Kersten, T.; Wolf, J.; Lindstaedt, M. Investigations Into the Accuracy of the UAV System DJI Matrice 300 RTK with the Sensors Zenmuse P1 and L1 in the Hamburg Test Field. In Proceedings of the XXIV ISPRS Congress "Imaging Today, Foreseeing Tomorrow", Nice, France, 6–11 June 2022; pp. 339–346. [CrossRef]
38. Acharya, B.S.; Bhandari, M.; Bandini, F.; Pizarro, A.; Perks, M.; Joshi, D.R.; Wang, S.; Dogwiler, T.; Ray, R.L.; Kharel, G.; et al. Unmanned Aerial Vehicles in Hydrology and Water Management: Applications, Challenges, and Perspectives. *Water Resour. Res.* **2021**, *57*, e2021WR029925. [CrossRef]
39. ROCK R3 Pro V2 | High-Accuracy LiDAR Scanner | ROCK Robotic. Available online: https://www.rockrobotic.com/r3pro-v2 (accessed on 19 June 2025).
40. UGRC—LiDAR Elevation Data. Available online: https://gis.utah.gov/products/sgid/elevation/lidar/#2016-bear-lake-bear-river-cache-valley--upper-weber-valley (accessed on 31 January 2026).

41. AeroPoints—Ground Control Points | Propeller. Available online: https://www.propelleraero.com/aeropoints/ (accessed on 19 June 2025).
42. Pan-Sharpening/Processing Data from Altum-PT and RedEdge-P Cameras in Agisoft Metashape—MicaSense Knowledge Base. Available online: https://support.micasense.com/hc/en-us/articles/4416696717847-Pan-sharpening-processing-data-from-Altum-PT-and-RedEdge-P-cameras-in-Agisoft-Metashape (accessed on 7 June 2026).
43. Americas—FloodList. Available online: https://floodlist.com/america (accessed on 19 June 2025).
44. Oakley, N.S.; Cannon, F.; Munroe, R.; Lancaster, J.T.; Gomberg, D.; Ralph, F.M. Brief Communication: Meteorological and Climatological Conditions Associated with the 9 January 2018 Post-Fire Debris Flows in Montecito and Carpinteria, California, USA. *Nat. Hazards Earth Syst. Sci.* **2018**, *18*, 3037–3043. [CrossRef]
45. Rengers, F.K.; Bower, S.; Knapp, A.; Kean, J.W.; vonLembke, D.W.; Thomas, M.A.; Kostelnik, J.; Barnhart, K.R.; Bethel, M.; Gartner, J.E.; et al. Evaluating Post-Wildfire Debris-Flow Rainfall Thresholds and Volume Models at the 2020 Grizzly Creek Fire in Glenwood Canyon, Colorado, USA. *Nat. Hazards Earth Syst. Sci.* **2024**, *24*, 2093–2114. [CrossRef]
46. Elhag, M.; Gitas, I.; Othman, A.; Bahrawi, J.; Gikas, P. Assessment of Water Quality Parameters Using Temporal Remote Sensing Spectral Reflectance in Arid Environments, Saudi Arabia. *Water* **2019**, *11*, 556. [CrossRef]
47. Kaplan, G.; Avdan, Z.Y.; Goncu, S.; Avdan, U. Evaluation of RapidEye-3 Satellite Data for Assessing Water Turbidity of Lake Borabey. In *Proceedings of the 4th International Electronic Conference on Water Sciences*; MDPI: Basel, Switzerland, 2019; p. 14.
48. Certificates of Waiver or Authorization (COA) | Federal Aviation Administration. Available online: https://www.faa.gov/about/office_org/headquarters_offices/ato/service_units/systemops/aaim/organizations/uas/coa (accessed on 24 June 2025).
49. Wienhold, K.J.; Li, D.; Li, W.; Fang, Z.N. Flood Inundation and Depth Mapping Using Unmanned Aerial Vehicles Combined with High-Resolution Multispectral Imagery. *Hydrology* **2023**, *10*, 158. [CrossRef]
50. Annis, A.; Nardi, F.; Petroselli, A.; Apollonio, C.; Arcangeletti, E.; Tauro, F.; Belli, C.; Bianconi, R.; Grimaldi, S. UAV-DEMs for Small-Scale Flood Hazard Mapping. *Water* **2020**, *12*, 1717. [CrossRef]
51. Muhadi, N.A.; Abdullah, A.F.; Bejo, S.K.; Mahadi, M.R.; Mijic, A. The Use of LiDAR-Derived DEM in Flood Applications: A Review. *Remote Sens.* **2020**, *12*, 2308. [CrossRef]
52. Tomsett, C.; Leyland, J. Using Repeat UAV-Based Laser Scanning and Multispectral Imagery to Explore Eco-Geomorphic Feedbacks along a River Corridor. *Earth Surf. Dyn.* **2023**, *11*, 1223–1249. [CrossRef]

Disclaimer/Publisher's Note: The statements, opinions and data contained in all publications are solely those of the individual author(s) and contributor(s) and not of MDPI and/or the editor(s). MDPI and/or the editor(s) disclaim responsibility for any injury to people or property resulting from any ideas, methods, instructions or products referred to in the content.